From Snapshot Maps to Continuous Monitoring of Global Forest Carbon at 100 m Resolution (2000–2025)

Yan Yang[1], Sassan Saatchi[1], Nich Kwon[1], Wen Tao Lin[1], Zhihua Liu[1], Shuang Li[1], Ricardo DalAgnol[1], Le Bienfaiteur Sagang[1]

[1] CTrees.org, Pasadena, California, CA, USA

Corresponding Author: yyang@ctrees.org

Preprint Status Statement: This manuscript is a non-peer-reviewed preprint submitted to EarthArXiv.

From Snapshot Maps to Continuous Monitoring of Global Forest Carbon at 100 m Resolution (2000–2025)

Yan Yang[1], Sassan Saatchi[1], Nich Kwon[1], Wen Tao Lin[1], Zhihua Liu[1],Ricardo DalAgnol[1], Le Bienfaiteur Sagang[1]

[1] CTrees.org, Pasadena, California, CA, USA

Corresponding Author: yyang@ctrees.org

Abstract

Accurate, high-resolution estimation of forest aboveground biomass (AGB) is critical for quantifying terrestrial carbon stocks and informing climate mitigation policy, yet existing global products remain constrained by coarse spatial resolution and limited temporal coverage that obscure sub-national-scale disturbances (Avitabile et al., 2016). This study presents a wall-to-wall global AGB product at 100 m native spatial resolution spanning 2000–2025, trained with a DenseNet architecture using independent AGB reference labels from ALS-derived AGB, field-plot and forest-inventory samples from the research community and selected regional/national inventories, and mangrove AGB training samples from global coastal regions. The predictor stack integrates Landsat surface reflectance time series (Chander et al., 2009; Roy et al., 2014; Zhu & Woodcock, 2012), ALOS PALSAR-1/2 L-band backscatter, GEDI and ICESat-2 canopy-height metrics used only as ancillary structural layers where valid 100 m aggregates are available, and topographic ancillary data (European Space Agency, 2021), employing spatial context windows (Kattenborn et al., 2021) to capture neighborhood-scale biomass gradients. Temporal harmonization is achieved through a buffered mask-aware correction strategy that excludes externally identified disturbance and activity areas from stable-pixel calibration, thereby preserving disturbance and regrowth signals while correcting broad cross-year biases. On a sample-level held-out validation/test set of approximately 1.01 million pixels compiled across eco-regions, the product achieves R^2 = 0.741, RMSE = 59.5 Mg ha^{-1}, and bias = −4.82 Mg ha^{-1}. Multi-decadal RGB change composites reveal spatially coherent carbon-dynamic patterns, including disturbance and recovery trajectories in southeastern Amazonia and regional biomass contrasts across major forest domains. These findings demonstrate that deep learning fusion of optical and SAR predictors with inventory-calibrated AGB reference labels and ancillary canopy-structure layers can support sub-kilometer global forest carbon monitoring, while spatial-block validation and public release of the processing provenance remain necessary before the product is used for formal reporting. **A more detailed research paper will be published soon.**

Keywords

aboveground biomass, remote sensing, deep learning, Landsat, ALOS PALSAR, airborne laser scanning, forest inventory, mangrove biomass, GEDI, ICESat-2, forest carbon, temporal change, global mapping

1. Introduction

1.1 From Carbon Snapshots to Continuous Monitoring

Forests constitute a major terrestrial carbon reservoir. The FAO Global Forest Resources Assessment 2025 estimates total forest carbon stock at approximately 714 Gt C across all pools, including 247 Gt C in aboveground biomass carbon (FAO, 2025). Forests also remain a persistent terrestrial sink: Pan et al. (2024) estimate a global forest carbon sink of 3.5 ± 0.4 Pg C yr^{-1} during the 2010s, while tropical deforestation offset roughly two-thirds of that sink benefit, approximately 2.2 ± 0.5 Pg C yr^{-1} during 1990–2019. These constraints shift the monitoring problem from static carbon snapshots toward continuous, spatially detailed estimation of biomass change through time, especially for annual management, disturbance, and regrowth processes that occur at hectare scale.

The international policy architecture for climate mitigation increasingly depends upon spatially explicit carbon stock data. The Paris Agreement's Global Stocktake, the REDD+ framework, and the Glasgow Leaders' Declaration on Forests and Land Use (UK Government, 2021), endorsed by more than 140 countries, require accurate estimates of forest carbon stocks and their changes. Countries participating in REDD+ are expected to compile greenhouse gas (GHG) inventories applying IPCC Tier 2 or 3 methodologies (IPCC, 2019), which demands country-specific emission factors and spatially disaggregated data.

Despite these clear policy needs, a persistent resolution gap limits the efficacy of existing global biomass products. The Global Climate Observing System (GCOS) lists AGB product requirements of 1000 m threshold, 100 m breakthrough, and 10 m goal horizontal resolution, with required two-sigma uncertainty targets of 30%, 20%, and 10%, respectively (GCOS, 2022). The ESA CCI Biomass project similarly targets 100 m AGB maps with relative error below 20% where AGB exceeds 50 Mg ha^{-1} (Santoro & Cartus, 2025). For many national and jurisdictional reporting applications, 100 m (1 hectare) or finer maps are therefore more useful than kilometer-scale products. Coarse-resolution products (>1 km) can dilute sub-grid disturbance processes including selective logging, fuelwood harvest, and non-stand-replacing fires, processes that operate at sub-hectare to hectare scales and contribute to forest carbon fluxes (Harris et al., 2021). Edge effects from forest fragmentation can reduce aboveground carbon stocks well beyond the cleared boundary; pan-tropical analyses report measurable losses up to 1.5 km from edges, and recent global mapping estimates approximately

70% of forest area lies within 1 km of an edge (Chaplin-Kramer et al., 2015; Yang et al., 2025).

1.2 Research Gap and Problem Statement

The landscape of existing global AGB products exhibits significant limitations in temporal continuity, spatial coverage, and native resolution. The ESA CCI Biomass product provides AGB maps at 100 m for 2007, 2010, and annually from 2015–2022 (Santoro & Cartus, 2025). The GlobBiomass product provided a global 2010 forest AGB map at approximately 1-ha resolution (Santoro et al., 2021). NASA GEDI provides 1-km gridded AGBD estimates for the GEDI sampling domain between about 51.6°S and 51.6°N (Healey et al., 2023). The ICESat-2 high-latitude boreal AGBD product provides circa-2020 30-m estimates by combining ATL08 lidar samples with HLS and Copernicus DEM covariates (Duncanson et al., 2023; Neuenschwander & Pitts, 2019). The JPL/Yu Global Biomass 2020 map provides 100-m live woody biomass estimates, with the public cloud-optimized GeoTIFF distributed through Zenodo (Yu et al., 2025). Xu et al. (2021) estimated spatially explicit global terrestrial live woody biomass changes from ground, airborne, and spaceborne observations for 2000–2019, demonstrating the importance of continuous biomass-stock change analysis rather than single-epoch stock mapping alone.

These products reveal three critical gaps. First, to our knowledge, no currently documented open product combines global wall-to-wall coverage, 100 m native resolution, and annual coverage through 2025 in a single 2000–2025 AGB stock time series. Second, existing products rely predominantly on semi-empirical backscatter inversion, gradient boosting, or Random Forest architectures that may not fully exploit the non-linear, spatially structured relationships among multi-sensor inputs. Third, temporal harmonization across sensor generations remains a persistent methodological challenge. Earlier work comparing field-based and remote-sensing biomass maps also emphasized that plot sampling bias, spatial support, and reference-data uncertainty must be treated explicitly rather than resolved by simple map averaging (Saatchi et al., 2015).

1.3 Contributions and Paper Organization

This paper presents a global wall-to-wall AGB product at 100 m spanning 2000–2025. The specific contributions are threefold: (1) to our knowledge, the first annual global 100 m AGB product spanning 26 years, trained from multi-source AGB reference labels compiled from ALS-derived, field/inventory, regional/national inventory, and mangrove AGB samples rather than GEDI/ICESat-2 AGBD labels; (2) a DenseNet-based regression workflow using 3 × 3 spatial context windows on fused optical, SAR, topographic, regional, and ancillary canopy-structure predictors; and (3) a time-series modeling and mask-aware harmonization workflow that preserves disturbance and regrowth signals while correcting broad cross-year biases.

The remainder of this paper is organized as follows. Section 2 reviews related work. Section 3 describes data sources and methods. Section 4 presents results. Section 5 discusses implications and limitations. Section 6 concludes.

2. Related Work

2.1 Global Aboveground Biomass Products

Early pan-tropical biomass maps. Saatchi et al. (2011) produced an early pan-tropical biomass/carbon map at 1-km resolution by calibrating GLAS waveforms with forest inventory data and extrapolating via maximum entropy modeling using MODIS spectral reflectance and radar backscatter imagery. Baccini et al. (2012) advanced this to approximately 463-m resolution using Random Forest. Avitabile et al. (2016) harmonized existing pantropical biomass maps with ground/reference data using regression-based correction, producing a 1-km fused map that reduced RMSE by 15–21% globally while still retaining regional artifacts from source products. However, at 463 m–1 km, these products can still miss or dilute selective logging, narrow degradation features, and small clearings that are important for carbon accounting. Sensor saturation in dense canopies remains a limitation across optical and microwave retrievals, though the saturation threshold differs by sensor and forest structure.

Low-frequency microwave retrieval studies show that radar sensitivity to AGB depends on wavelength, incidence angle, canopy density, and forest structural variability (Saatchi, Marlier, et al., 2011). GlobBiomass later provided an approximately 1-ha global 2010 AGB product using combined SAR and optical imagery (Santoro et al., 2021). However, L-band backscatter alone loses sensitivity in high-biomass forests, particularly above approximately 150 Mg ha^{-1} depending on forest structure and site conditions. P-band SAR is expected to improve sensitivity in high-biomass forests, but long, consistent P-band time series are not yet available for the full 2000–2025 period addressed here.

Multi-sensor fusion. ESA CCI Biomass (v6.0) provides global AGB at 100 m for 2007, 2010, and 2015–2022 from C-band and L-band SAR calibrated with GEDI and ICESat-2 (Santoro & Cartus, 2025). The JPL/Yu 2020 global live woody vegetation biomass map provides a 100 m 2020 biomass product, with the public cloud-optimized GeoTIFF distributed through Zenodo (Yu et al., 2025). The NCEO Africa product provides 100 m AGB for mapped epochs in 2007–2010 and 2015–2020 via Random Forest, achieving RMSE = 48.5 Mg ha^{-1} and R^2 = 0.83 in initial independent validation (Committee on Earth Observation Satellites, 2024). A recent review confirms that integrating optical, SAR, and lidar data provides one of the most robust frameworks for AGB estimation (Tian et al., 2023).

2.2 Reference AGB Labels and Ancillary Spaceborne LiDAR

Reference AGB labels for this product are not derived from GEDI or ICESat-2 AGBD products, which are modeled products with regionally varying uncertainty. Instead, the target variable is compiled from ALS-derived AGB, field-plot and sample forest-inventory data from the research community and selected regional/national inventories, and mangrove AGB training samples across global coastal regions. This design keeps the supervised target tied to inventory-calibrated AGB reference data while allowing GEDI

and ICESat-2 canopy-height metrics to serve only as ancillary structural predictors where valid 100 m aggregates are available.

Spaceborne lidar remains useful in the predictor stack, but only as ancillary structural information. GEDI collects full-waveform lidar data between 51.6°S and 51.6°N, with relative-height metrics such as RH50, RH75, RH90, and RH98 describing vertical canopy structure (Dubayah et al., 2020). ICESat-2 ATL08 provides photon-counting lidar height metrics at high latitudes and other regions where valid observations are available (Neuenschwander & Pitts, 2019). These GEDI and ICESat-2 canopy-height metrics are aggregated to the 100 m grid where quality-filtered observations exist and are used as optional ancillary training layers, not as the source of AGB target labels.

The spatial distribution of the compiled reference samples is summarized in Fig. 1. Field-derived samples and ALS/lidar-derived samples provide complementary geographic coverage but remain spatially uneven, motivating the use of eco-region covariates, region-aware quality control, and explicit provenance reporting during model development.

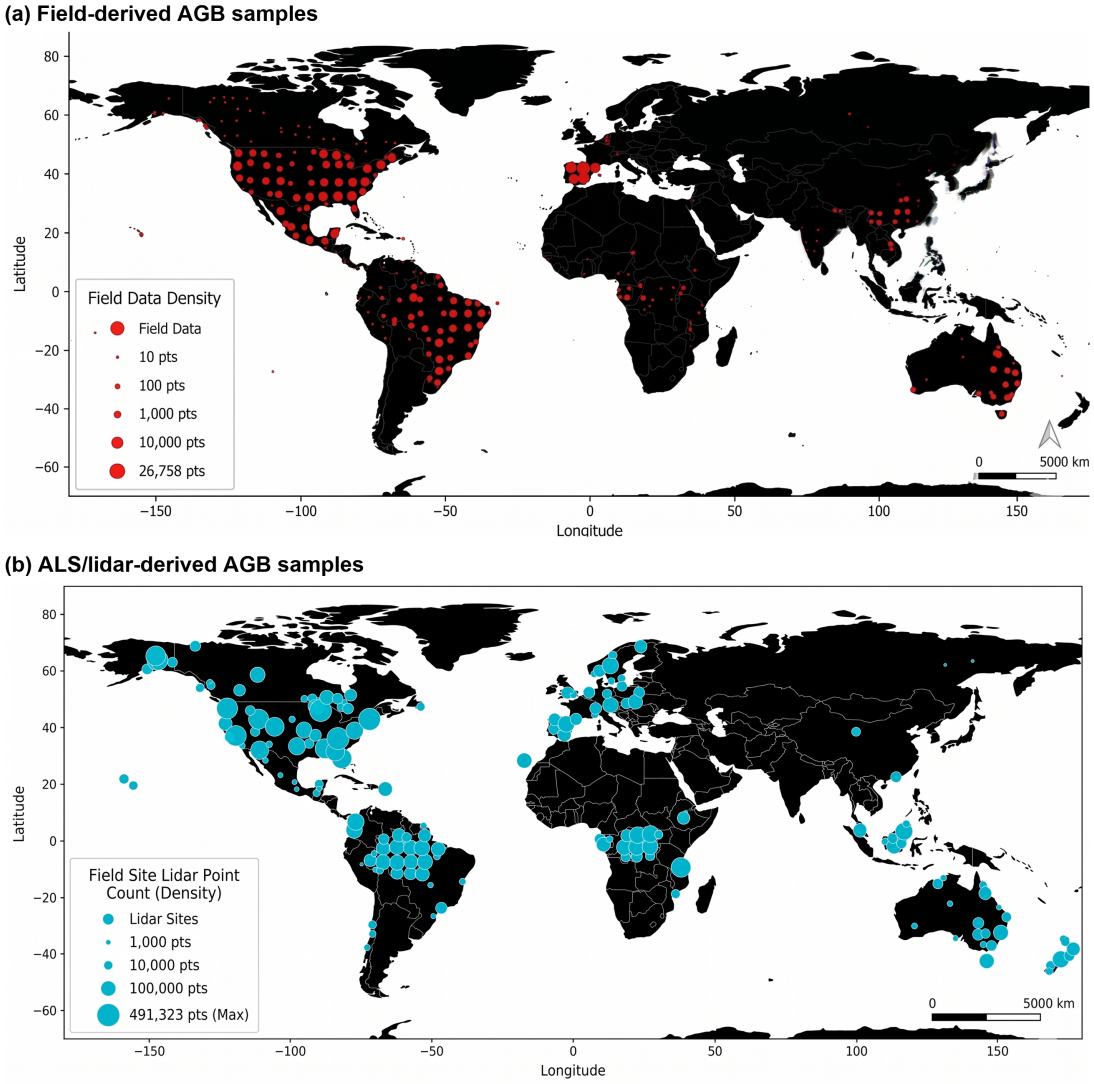

Figure 1. Global distribution and density of training/reference AGB samples used to construct the 100 m product. (a) Field-derived samples compiled from field plots and forest-inventory sources. (b) ALS/lidar-derived samples converted to AGB density at hectare-scale support where available. Symbol size indicates the relative number of samples or points within each mapped location/bin.

2.3 Deep Learning for Biomass Estimation

CNNs have emerged as powerful tools for remote sensing regression. Potapov et al. (2021) produced the first global 30-m canopy height map for 2019 by integrating GEDI RH95 with Landsat reflectance. Lang et al. (2023) developed a probabilistic deep learning model producing the first global 10-m canopy height map by fusing GEDI with Sentinel-2, trained on 600 million samples. Patch-based CNN approaches extract local spatial context through input windows to capture neighborhood spatial autocorrelation. DenseNet architectures offer particular advantages for geospatial regression: dense connectivity enables maximum feature reuse, strengthens gradient flow, and can outperform residual-network baselines in limited-sample regimes (Huang et al., 2017).

Scaling to global products requires TFRecord pipelines and GPU-accelerated distributed computing.

2.4 Temporal Change Detection and Harmonization

The Hansen GFC dataset defines forest loss as stand-replacement disturbance at approximately 30-m resolution with annual loss-year layers (Hansen et al., 2013). GABAM provides 30-m global annual burned-area data from Landsat time series, with recent Zenodo releases extending the record through 2024 (Long et al., 2019; Zhang et al., 2025). The JRC TMF dataset provides 30-m wall-to-wall maps of degradation and deforestation for tropical moist forests from 1990 onward, differentiating temporary degradation from permanent deforestation (Vancutsem et al., 2021). Radiometric normalization across multi-temporal imagery is essential; pseudo-invariant features (PIFs), histogram matching, and CCDC structural break detection are established methods. For biomass applications, disturbance masks should be buffered or otherwise expanded because selective logging infrastructure and edge effects can affect areas larger than the directly cleared patches.

3. Materials and Methods

The end-to-end workflow is summarized in Fig. 2. It is organized into three modules: (1) canopy-height mapping and eco-cluster generation, (2) 2020 base AGB mapping and validation, and (3) annual change detection and temporal harmonization. Module 1 builds ancillary canopy-structure layers from quality-filtered spaceborne lidar and remote-sensing predictors; Module 2 trains the 2020 AGB model using independent AGB reference labels; and Module 3 extends predictions through the 2000–2025 annual time series with disturbance-aware temporal harmonization.

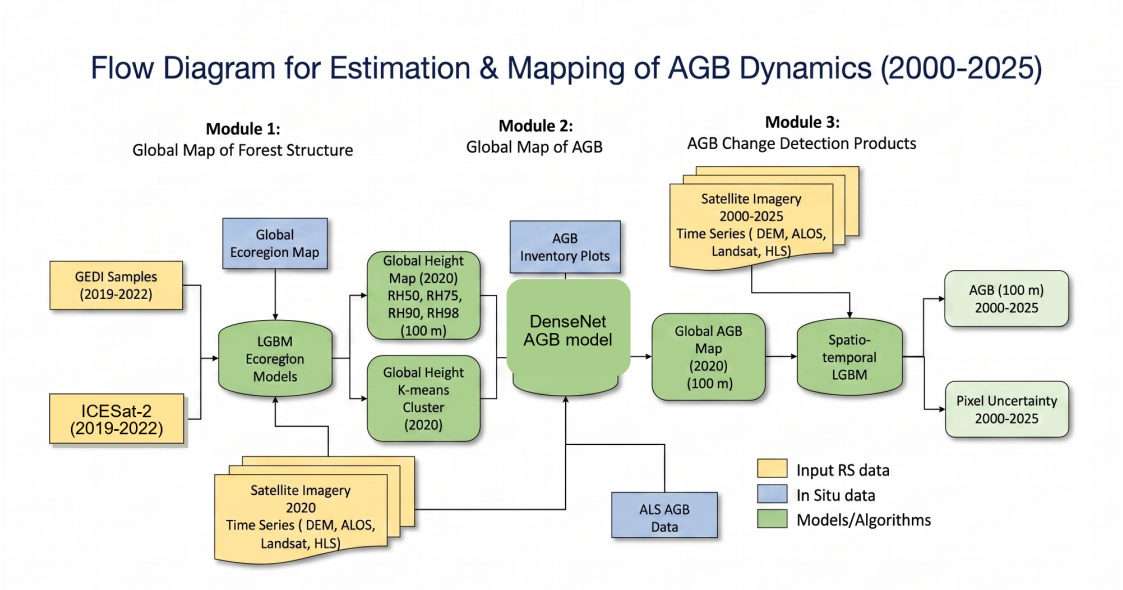

Figure 2. Methodological workflow organized into Module 1 (canopy-height mapping and eco-cluster generation), Module 2 (2020 base AGB mapping and validation), and Module 3 (annual AGB change detection from 2000 to 2025). GEDI and ICESat-2 samples support ancillary 100 m canopy-structure

layers rather than target labels, while field/inventory, ALS-derived, and mangrove AGB samples train the DenseNet AGB model. Annual optical/SAR/topographic composites and disturbance masks support time-series extension and pixel-level uncertainty estimation.

3.1 Study Area and Target Variable

The product covers global vegetated land areas at 100 m spatial resolution. The target variable is aboveground biomass density (AGB, Mg ha^{-1}). Target labels are compiled from ALS-derived, field/inventory, regional/national inventory, and mangrove AGB reference samples; the detailed label-preparation workflow is described in Section 3.4. GEDI and ICESat-2 canopy-height metrics are not converted to AGB labels in this workflow and are used only as ancillary structural covariates where valid aggregated 100 m data exist. A valid target-label range of 0–800 Mg ha^{-1} is enforced during sample extraction and final masking as an internal quality-control threshold for extreme or invalid labels, not as a published GEDI product limit or a biophysical maximum.

3.2 Input Data

Table 1 summarizes the input predictor variables. Optical predictors comprise Landsat Level 2 Collection 2 Tier-1 (L5/L7/L8/L9) surface reflectance (Chander et al., 2009; Roy et al., 2014), atmospherically corrected from 2000 onwards. Bands selected for their atmospheric robustness include red, near-infrared (NIR), and short-wave infrared (SWIR1, SWIR2), quality-filtered using Landsat cloud and cloud-shadow masks (Zhu & Woodcock, 2012). For the 2020 anchor map, the Harmonized Landsat-Sentinel-2 (HLS) dataset provides consistent high-resolution surface reflectance by combining Landsat and Sentinel-2 sensors (Claverie et al., 2018). SAR predictors include ALOS PALSAR L-band Fine-Beam Dual-polarization (FBD) HH and HV backscatter coefficients and their standard deviations (HHstd, HVstd) (Shimada et al., 2014), providing deep canopy penetration to capture woody structure; standard deviation layers quantify local structural heterogeneity. GEDI and ICESat-2 relative-height metrics are included only as ancillary canopy-structure predictors where quality-filtered observations can be aggregated to the 100 m grid as described in Section 2.2. Topographic predictors from the Copernicus DEM GLO-30 (European Space Agency, 2021) were aggregated to 100 m to derive mean elevation and elevation standard deviation (DEMstd), accounting for slope and surface roughness influences on biomass distribution. Ancillary predictors include Copernicus tree cover fraction (Buchhorn et al., 2020) for vegetation structure, and global eco-cluster regions with coordinate grids (x_grid, y_grid) generated via np.meshgrid to facilitate regional model adaptation by bioclimatic zone. All gridded predictors are aligned to the 100 m analysis grid before modeling. Optical predictors are represented as annual cloud-filtered composites, and higher-resolution layers are aggregated or summarized to 100 m using band-appropriate statistics such as mean reflectance or height metrics, local standard deviations, and proportional disturbance or tree-cover summaries so each model sample has consistent annual 100 m support.

Table 1. Input predictor variables for the 2020 anchor and annual AGB models.

Layer group	Variables	Description	Source Resolution	Strategic contribution
ALOS PALSAR	HH, HV, HHstd, HVstd	L-band backscatter and standard deviation	25 m	Deep canopy penetration; structural heterogeneity
HLS / Landsat	RED, NIR, SWIR1, SWIR2 + VI + std	Surface reflectance and vegetation indices	30m	Chlorophyll, moisture, forest-type differentiation
Spaceborne lidar structure	GEDI RH metrics; ICESat-2 ATL08 RH metrics	Aggregated canopy-height and relative-height metrics used only as ancillary predictor layers where valid 100 m observations exist	100 m aggregate	Structural covariate support; not used as AGB target labels
Topographic	DEM, DEMstd	Elevation mean and standard deviation	30 m	Slope, roughness, environmental normalization
Regionality	Cluster, x_grid, y_grid	Eco-clusters and coordinates	100 m	Regional bioclimatic adaptation
Copernicus	Tree cover fraction	Vegetation structure	100 m	Forest-density proxy

3.3 Disturbance Data for Temporal Processing

Table 2 lists the disturbance products used for temporal harmonization. Hansen GFC forest loss (Hansen et al., 2013) characterizes stand-replacement disturbance at 30 m from 2001 onward. GABAM burned area (Long et al., 2019; Zhang et al., 2025) provides 30-m annual burned-area maps, with recent releases extending the record through 2024. The JRC TMF dataset (Vancutsem et al., 2021) provides 30-m degradation and deforestation maps for tropical moist forests from 1990 onward. These 30-m disturbance layers are aggregated to 100 m while maintaining the proportion of each disturbance type within each pixel. For temporal harmonization, pixels flagged by these activity layers or by internal change-detection masks are excluded from the stable-pixel calibration pool. Cross-year normalization is therefore estimated from pixels most likely to remain unchanged, while disturbed pixels remain available to retain real loss and regrowth signals.

Table 2. Disturbance products used for mask-aware temporal harmonization.

Product	Layer description	Source Resolution	Temporal extent
Hansen GFC	Forest loss (stand-replacement)	30 m	2001–present
GABAM	Burned area	30 m	2014–2024 (v3)
JRC TMF	Deforestation and degradation (tropics)	30 m	1990 onward (tropics)

3.4 Target Variable Preparation

Reference AGB labels are assembled independently of GEDI and ICESat-2 AGBD products. ALS-derived AGB, field/inventory samples, selected regional/national inventory records, and mangrove AGB training samples are converted or harmonized to AGB density units (Mg ha^{-1}), assigned to the 100 m analysis grid, and screened for geolocation, forest-cover consistency, missing predictors, and extreme values. The compiled label set therefore represents a multi-source AGB reference sample rather than a single sensor product. Fig. 1 summarizes the geographic distribution of these reference sources; source provenance, region, date or epoch, spatial support, conversion method, and quality-control flags are intended for supplementary provenance tables so users can evaluate spatial heterogeneity in the training labels. GEDI L2A relative-height metrics and ICESat-2 ATL08 height metrics are handled separately as ancillary structural predictor layers where valid 100 m aggregates exist; missing or unavailable aggregates are treated as missing ancillary covariates rather than missing target labels.

3.5 Module 2: Base AGB Model Architecture

Module 2 uses a DenseNet-based regressor as the core predictive engine for 2020 base AGB mapping. DenseNet was selected for this geospatial task because its dense connectivity pattern, which concatenates feature maps from all preceding layers, facilitates maximum feature reuse and superior gradient flow (Huang et al., 2017). This is particularly advantageous for biomass estimation, where (1) multi-modal inputs (radar backscatter, multi-spectral reflectance, topographic data, and ancillary canopy-height layers) contain structurally different feature types that benefit from preserved diversity across layers; (2) training labels are spatially sparse and heterogeneous, reflecting the availability of ALS-derived AGB, inventory samples, and mangrove AGB estimates rather than uniform global coverage; and (3) spatial autocorrelation in forest structure means that neighborhood context carries predictive signal that deeper concatenated features can exploit.

The network uses a custom DenseNet variant with growth rate k = 8 and (8, 12) dense blocks, followed by global average pooling and fully connected regression heads (Dense(64) with ReLU, Dense(1) linear output), comprising approximately 112,000–113,000 trainable parameters depending on the input-band stack. This compact architecture was chosen over standard DenseNet-121 (~8 M parameters) to reduce overfitting given the heterogeneous, spatially sparse reference AGB training data. A 3 ×

3 spatial context window is applied so that each prediction incorporates the spatial neighborhood surrounding the target pixel. This captures forest edge transitions, canopy heterogeneity, and local structural texture more indicative of woody biomass than isolated pixel values. The available notebooks document 3 × 3 patch extraction and TFRecord serialization. Additional smoothing or speckle filtering is treated as preprocessing metadata and is not claimed here as part of the fixed model architecture unless documented in reproducible preprocessing scripts.

3.6 Training Pipeline

Data are partitioned using a nested 80/20 strategy documented in the processing notebooks: the initial dataset reserves 20% for held-out testing; the remaining 80% is split again with 20% reserved for evaluation/hyperparameter tuning, yielding 64% training, 16% validation, and 20% test. Multi-modal layers are tiled into synchronized 3 × 3 spatial stacks. Raw arrays are serialized into TFRecords, a high-performance binary format that optimizes GPU throughput. TFRecords are generated per eco-cluster to support regional representation during stochastic gradient descent. The pipeline removes pixels with missing data or values outside the 0–800 Mg ha^{-1} range. Features are standardized per band using training-set mean and standard deviation computed within each eco-cluster. The model is trained with MAE loss, RMSE as a monitoring metric, and early stopping on validation loss. Because this split is random rather than geographic, the reported metrics are sample-level and should be complemented by spatial-block validation before formal claims about geographic transferability.

3.7 Module 3: Time-Series Modeling and Change Detection (2000–2025)

Module 3 extends the 2020 base map into annual AGB estimates and change products through four stages.

(1) 2020 anchor prediction: A multi-band stack combining ALOS PALSAR-2 HH/HV, HLS red/NIR/SWIR1/SWIR2, vegetation indices, DEM variables, eco-cluster coordinates, and valid aggregated GEDI/ICESat-2 canopy-height metrics where available is predicted tile-by-tile to generate the base 2020 AGB map. The spaceborne-lidar layers are ancillary predictors; they do not define the target AGB labels.

(2) Annual Landsat prediction: For each year 2000–2025, Landsat optical predictors are combined with static or slowly varying ancillary layers such as DEM, eco-cluster coordinates, ALOS PALSAR-derived structure where available, and valid aggregated GEDI/ICESat-2 canopy-height metrics where available. Predictions are generated at 100-m resolution with 3 × 3 context windows using the trained DenseNet. HLS data are used only for the 2020 anchor and for years where Sentinel-2 overlap exists (2015 onwards); pre-2015 annual maps rely on Landsat-5/7 optical time series plus the available ancillary layers.

(3) Residual bias correction: A second DenseNet with the same architecture is trained to predict residual structure from the 2020 anchor model and is then applied to annual predictions to reduce systematic deviations associated with

sensor-specific artifacts (for example, Landsat versus HLS bandpass differences or PALSAR-1 versus PALSAR-2 calibration offsets). Because an independent residual-model benchmark is not yet available, this manuscript does not claim a fixed percentage improvement from the residual correction step.

(4) Mask-aware temporal harmonization: A buffered activity mask derived from Hansen GFC loss, GABAM burn area, JRC TMF disturbance layers, and the project's internal activity mask separates pixels into stable and disturbed/activity-affected classes. Stable pixels are used to anchor cross-year histogram matching and change-detection correction to the 2020 baseline. Disturbed pixels are withheld from the stable-pixel calibration pool so genuine biomass loss or gain signals are less likely to be smoothed away by cross-year normalization. This separation is critical because uniform histogram matching across all pixels would artificially dampen deforestation and regrowth signals by compressing their distributions toward the 2020 mean.

3.8 Validation and Uncertainty

Validation aggregates approximately 1.01 million predictions across eco-region strata. Primary metrics include R^2, RMSE, bias, and MAE. Residuals are analyzed by predicted AGB bins to assess heteroscedasticity. The RGB change composite is interpreted using the Fig. 7 color scheme: red/yellow for early/late deforestation, blue/cyan for growth, green for early regrowth followed by late loss, and magenta for early loss followed by regrowth.

3.8.1 Validation Design and Spatial Dependence

The available processing notebooks document a random nested train/validation/test split rather than a spatial block holdout. Reported metrics (R^2, RMSE, bias) therefore evaluate performance on held-out pixels from the compiled sample set and are reported here as sample-level validation. Because 3 × 3 spatial windows and eco-cluster stratification introduce spatial autocorrelation, these metrics may overstate geographic transferability if nearby pixels from the same landscapes occur in different splits. A spatial-block experiment, such as holding out entire geographic tiles or eco-regions, remains a required robustness test before describing the evaluation as spatially independent.

4. Results

4.1 Global AGB Distribution (2020)

The global AGB map for 2020 (Fig. 3) reveals the expected spatial pattern of terrestrial biomass, with the highest values concentrated in tropical rainforests. The Amazon Basin, Congo Basin, and insular Southeast Asia exhibit contiguous high-biomass areas (>300 Mg ha^{-1}), reflecting the structural dominance of moist tropical forests. Boreal forests across North America and Eurasia show lower but spatially extensive biomass (50–150 Mg ha^{-1}), while temperate zones and dryland ecosystems display intermediate values.

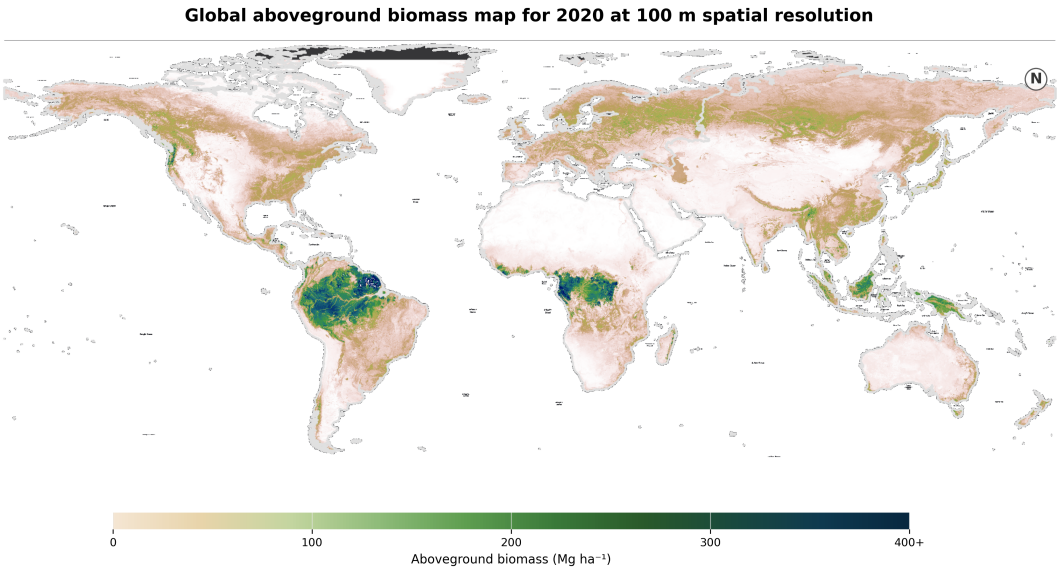

Figure 3. Global aboveground biomass map for 2020 at 100 m spatial resolution. Highest biomass values are observed in tropical rainforests of the Amazon Basin, Congo Basin, and Southeast Asia, with lower but extensive biomass in boreal forests of North America and Eurasia.

4.2 Validation Results

The held-out test-set evaluation (n ≈ 1.01 million pixels) yields R^2 = 0.741, RMSE = 59.5 Mg ha^{-1}, and bias = −4.82 Mg ha^{-1} (Fig. 4a). The density-colored scatter plot shows that the product captures the central tendency of AGB across the main biomass range, with predictions clustering around the 1:1 line at low-to-moderate biomass (0–200 Mg ha^{-1}). Spread increases at higher biomass, consistent with optical/SAR saturation and fewer high-biomass reference samples. The residual boxplot (Fig. 4b) shows increasing variance in the highest biomass bins, indicating that uncertainty grows in dense-canopy conditions even though the overall bias remains small.

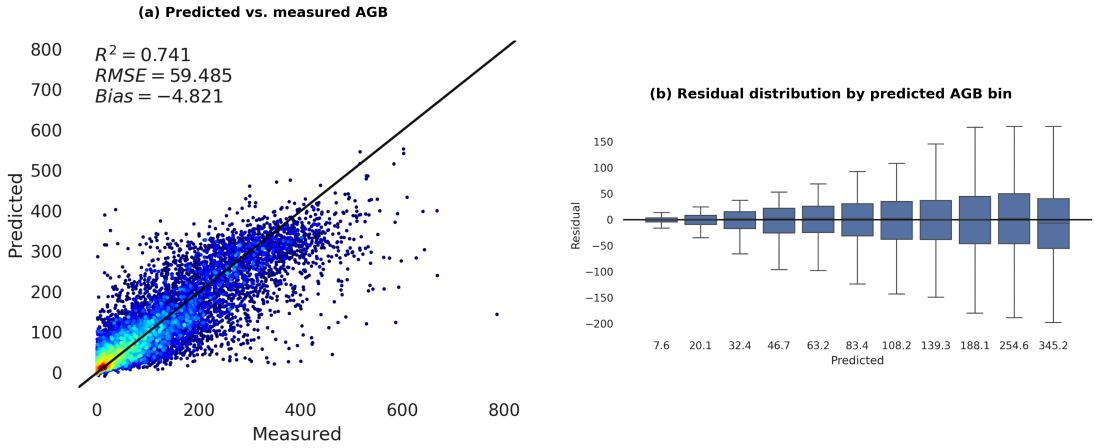

Figure 4. (a) Scatter plot of predicted versus measured AGB on the held-out test set, with density coloring revealing strongest agreement at low-to-moderate biomass. Metrics: R^2 = 0.741, RMSE = 59.5 Mg ha^{-1}, bias = −4.82 Mg ha^{-1}. (b) Boxplot of residuals stratified by predicted AGB bins (0–15, 15–30, 30–45, 45–60, 60–80, 80–100, 100–125, 125–150, 150–200, 200–300, >300 Mg ha^{-1}), showing increasing variance at high biomass consistent with sensor saturation.

Biome-stratified validation indicates that performance varies across forest types (Fig. 5). Tropical moist forests show the strongest biome-level agreement among the four forest panels (R^2 = 0.692, RMSE = 74.6 Mg ha^{-1}) but retain the largest absolute errors because high-biomass canopies extend beyond the most sensitive range of optical-SAR predictors. Tropical dry forests show lower RMSE and MAE (35.8 and 19.4 Mg ha^{-1}) over a lower biomass range, while temperate forests show weaker explanatory power (R^2 = 0.426), consistent with heterogeneous stand structure and management history. Boreal forests show moderate correlation (R^2 = 0.528) and near-zero bias (−0.6 Mg ha^{-1}), indicating relatively balanced errors within a narrower biomass range.

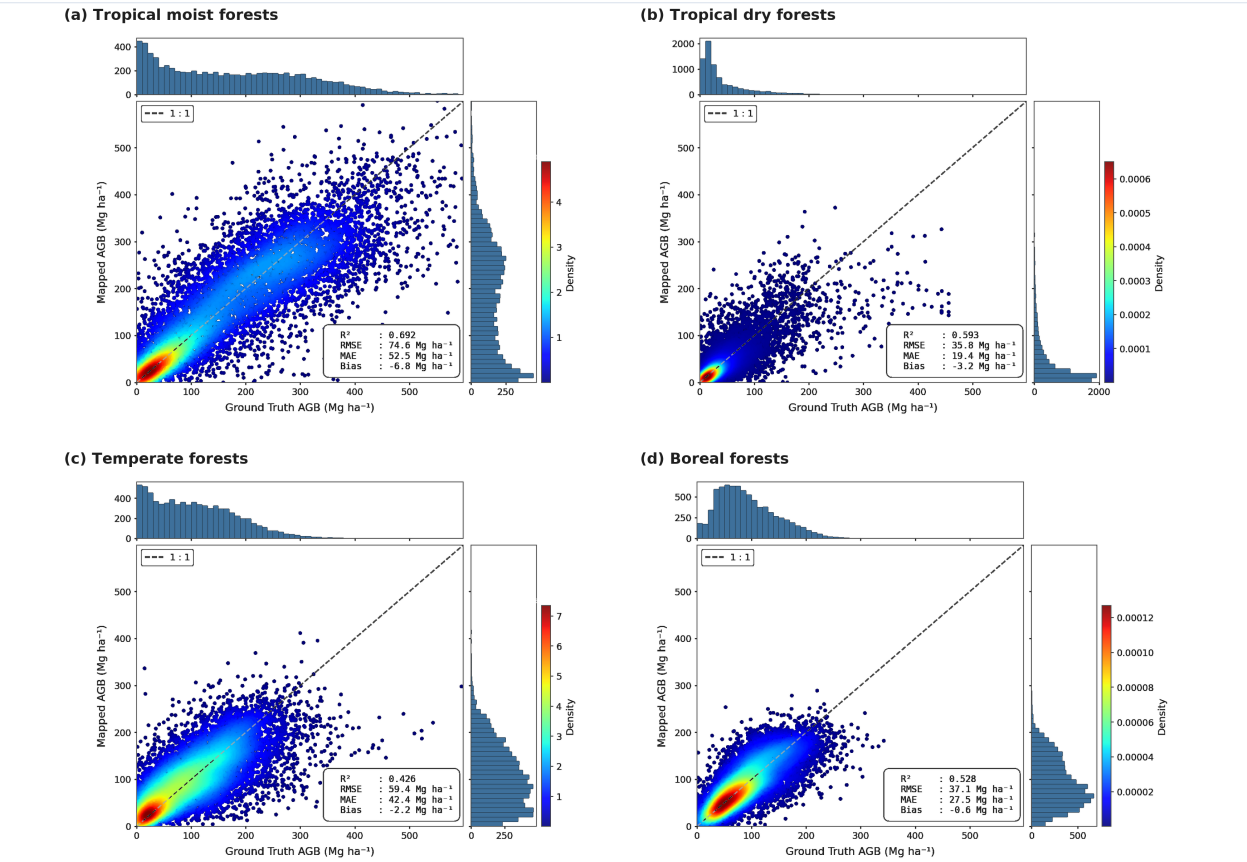

Figure 5. Biome-stratified validation scatter plots for forest biomes. Panels show mapped AGB versus reference AGB for (a) tropical and subtropical moist broadleaf forests, (b) tropical and subtropical dry broadleaf forests, (c) temperate broadleaf and mixed forests, and (d) boreal forests/taiga. Density colors indicate sample concentration, marginal histograms show the distributions of reference and mapped AGB, and dashed lines show the 1:1 relationship. Total reference sample counts available for panels (a)-(d) are 1,744,964, 237,363, 331,705, and 452,583, respectively; each panel displays 8,000 plotted samples.

4.3 Regional Detail

Four regional subsets illustrate, rather than independently validate, the spatial fidelity of the 100-m product. In the Amazon Basin (Fig. 6a), high biomass (>300 Mg ha^{-1}) dominates the central and western intact forest, with pronounced low-biomass patterns along the southern and eastern margins consistent with the Arc of Deforestation. Riparian corridors of elevated biomass trace major river systems, while anthropogenic clearings appear as sharp low-biomass patches. In Central Africa (Fig. 6b), the Congo Basin exhibits strong biomass gradients from the high-density forest core in northeastern DRC to lower-biomass transition zones, with linear low-biomass features that are consistent with logging-road or access-corridor degradation. Southeast Asia (Fig. 6c) shows insular fragmentation: patches of high-biomass intact forest are embedded within matrices of low-biomass plantation or agricultural land cover, particularly in Borneo and Sumatra. In Western North America (Fig. 6d), high-biomass coastal forests contrast with lower-biomass interior landscapes; irregular low-biomass patches are consistent with stand-replacing fire or harvest disturbance. The panels are

interpreted as qualitative spatial examples; formal attribution of specific disturbance mechanisms requires panel bounding boxes, activity-layer overlays, and independent regional reference data.

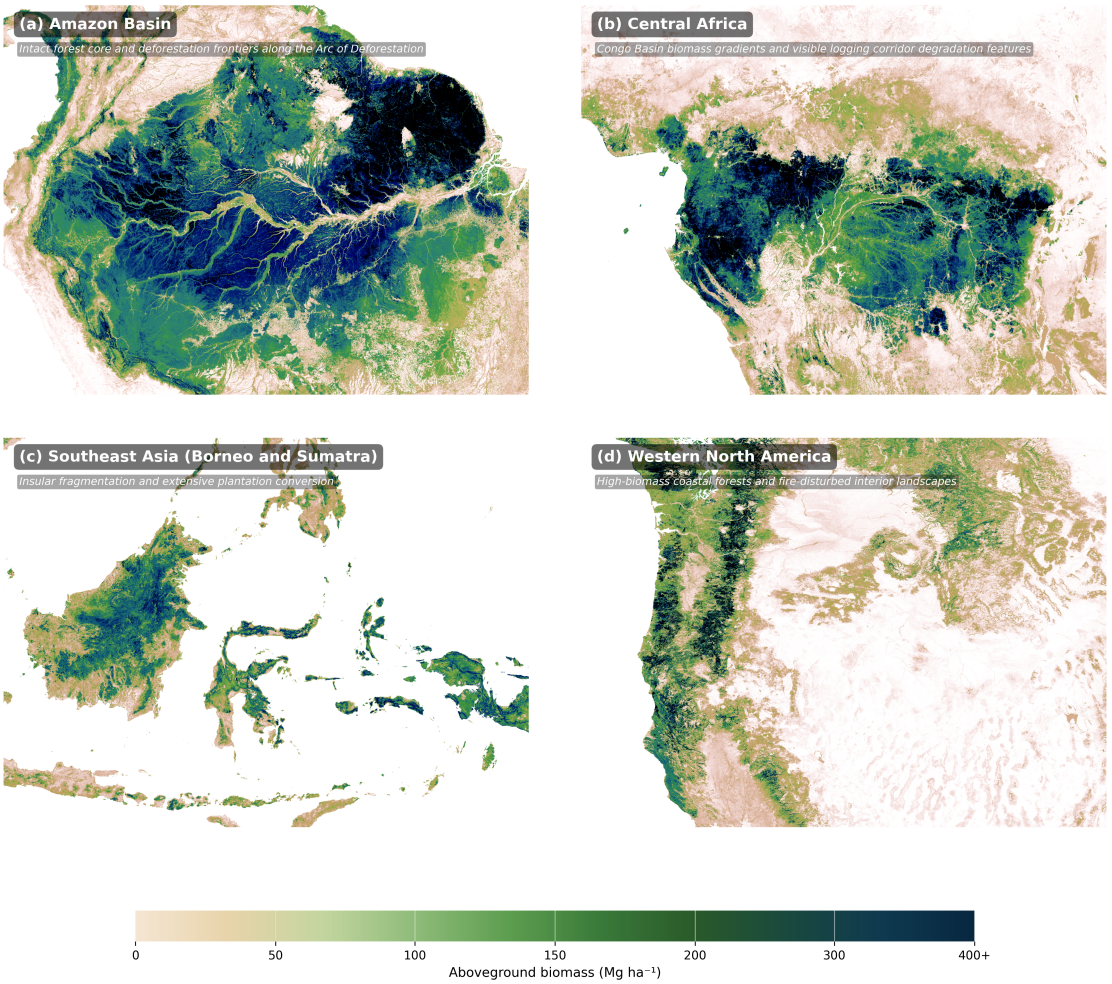

Figure 6. Regional detail at 100 m resolution. (a) Amazon Basin with intact forest core and low-biomass patterns along the Arc of Deforestation. (b) Central Africa with Congo Basin biomass gradients and linear low-biomass corridor features. (c) Southeast Asia (Borneo and Sumatra) showing insular fragmentation and extensive low-biomass land-cover conversion. (d) Western North America with high-biomass coastal forests and lower-biomass disturbed interior landscapes. The panels are qualitative regional examples rather than independent validation datasets.

4.4 Change Dynamics (2000–2025)

Change detection is a central use case of the annual product. The RGB change composite (Fig. 7a) condenses 26 annual AGB estimates into a single view of disturbance and recovery for the southeastern Amazonia sub-region shown in panel (a). The panel highlights spatially coherent early and late deforestation, regrowth, and stable high-biomass areas, while the temporal profiles in Fig. 7b–g show representative pixel trajectories underlying these colors.

Temporal profiles from illustrative pixels collected within the southeastern Amazonia sub-region shown in Fig. 7a are plotted in Mg ha^{-1}, showing distinct disturbance and recovery signatures. Early deforestation (Fig. 7b) shows an abrupt step-function drop from ~224 to ~22 Mg ha^{-1} around 2005, consistent with stand-replacement land conversion followed by stable low-biomass land cover (pasture/cropland). Residual biomass may reflect woody regrowth and scattered trees below the detection threshold of stand-replacement algorithms. Multi-year deforestation (Fig. 7c) exhibits gradual decline over 8–10 years, consistent with progressive degradation through selective logging or repeated fires. Late deforestation (Fig. 7d) remains stable at >270 Mg ha^{-1} through 2016 before dropping sharply by 2017, indicating recent clearing. For recovery dynamics, late-year growth (Fig. 7e) remains near zero through 2020 and increases to ~89 Mg ha^{-1} by 2025. The early loss + regrowth pattern (Fig. 7f) drops from ~103 Mg ha^{-1} to a low-biomass phase after 2003 and recovers after 2021 to ~73 Mg ha^{-1} by 2025, consistent with local disturbance followed by secondary regrowth. The continuous growth profile (Fig. 7g) shows sustained increase from ~48 to ~174 Mg ha^{-1} over 2000–2025 within the same southeastern Amazonia sample area, consistent with localized biomass gain or regrowth. These trajectories are interpreted as illustrative examples unless each pixel is linked to coordinates and corroborating disturbance or land-cover evidence. Similar disturbance and recovery interpretations are consistent with Amazon studies that used lidar/radar observations to quantify post-drought biomass loss and secondary-forest carbon uptake (Yang et al., 2018, 2020).

Together, the composite and profiles show that the annual product retains temporally coherent change behavior rather than only reproducing static spatial biomass gradients. Abrupt clearing, gradual decline, post-disturbance recovery, and stable high-biomass trajectories are separable in the profiles, supporting use of the product to screen candidate disturbance and regrowth areas at 100 m resolution. Formal change attribution remains a separate validation step requiring coordinates, independent disturbance layers, and land-cover evidence.

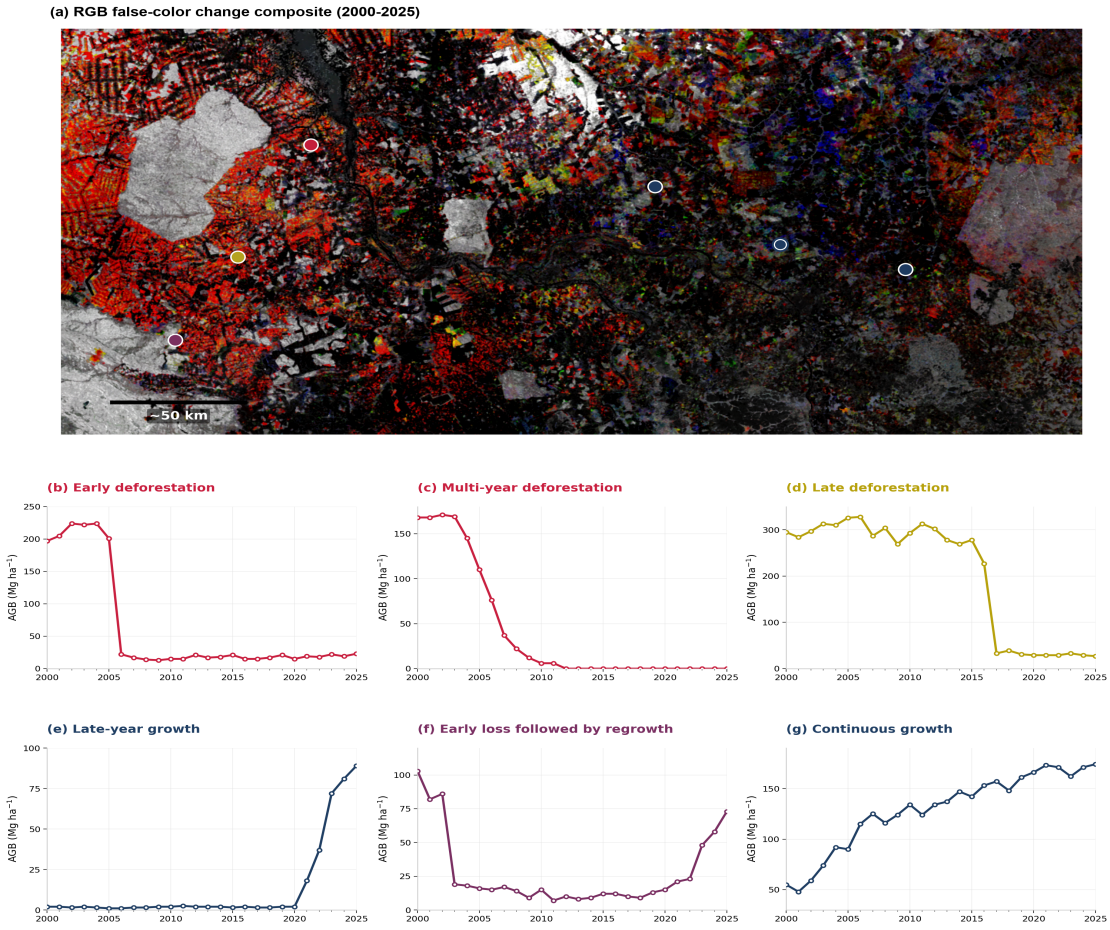

Figure 7. (a) RGB false-color change composite for the southeastern Amazonia sub-region used for all profile samples, encoding biomass dynamics from 2000–2025. Red = early deforestation (2000–2008); yellow = late deforestation (2017–2025); blue = late-period growth; green = early regrowth followed by late loss; magenta = early loss followed by regrowth. Cyan indicates continuous growth. Inset shows location within South America (black rectangle). Scale bar: ~50 km. High-resolution canopy height models provide complementary structural context for interpreting these change composites (Lang et al., 2023). (b)-(g) Temporal profiles of AGB (Mg ha^{-1}) for representative pixel locations collected from the southeastern Amazonia sub-region shown in panel (a). (b) Early deforestation: abrupt biomass drop from ~224 to ~22 Mg ha^{-1} around 2005, diagnostic of stand-replacement conversion followed by stable low-biomass land cover. (c) Multi-year deforestation: gradual decline over 8–10 years, consistent with progressive degradation through selective logging or repeated fires. (d) Late deforestation: stable high biomass through 2016, then a sharp drop by 2017 indicating recent clearing activity. (e) Late-year growth: near-zero values through 2020 followed by growth to ~89 Mg ha^{-1} by 2025, characteristic of secondary forest regrowth. (f) Early loss followed by regrowth: biomass drops to a low-biomass phase after 2003, then recovers to ~73 Mg ha^{-1} by 2025, consistent with local disturbance followed by secondary regrowth. (g) Continuous growth: sustained increase from ~48 to ~174 Mg ha^{-1} over 2000–2025 within the same southeastern Amazonia sample area, indicating localized biomass gain or regrowth.

5. Discussion

5.1 Hectare-Scale Carbon Dynamics

The 100-m resolution of this product enables detection of carbon losses from disturbances smaller than a 1-km grid cell that would otherwise be diluted in coarser products. Xu et al. (2021) estimated spatially explicit global terrestrial live biomass changes from ground, airborne, and spaceborne observations for 2000–2019, demonstrating the value of fine spatial detail and repeated observations for tracking forest carbon dynamics. Edge effects from fragmentation can depress AGB near forest edges, with pan-tropical analyses reporting losses extending up to 1.5 km and recent global mapping estimating approximately 16% lower AGB near edges and about 70% of forest area within 1 km of an edge (Chaplin-Kramer et al., 2015; Yang et al., 2025). At 100-m resolution, these edge gradients are partially resolved, whereas 1-km products average them into a single mixed pixel with substantially reduced sensitivity to actual carbon stock changes (Baccini et al., 2012). The RGB composites demonstrate that the product captures not only stand-replacement deforestation but also the subtler spectral signatures of degradation and regrowth, enabling attribution of biomass change to specific disturbance types when combined with the activity data layers (Table 2).

5.2 Uncertainty and Limitations

Several sources of uncertainty constrain the accuracy of this product. Optical saturation: Landsat spectral indices saturate over high leaf area index, constraining discrimination above 300–400 Mg ha^{-1} in dense tropical forests. SAR saturation: L-band HV backscatter loses sensitivity particularly above approximately 150 Mg ha^{-1} depending on forest structure, though fusion with optical, topographic, and ancillary canopy-height predictors mitigates this through complementary information. Reference-label uncertainty: The direct-regression approach does not eliminate uncertainty in the target data. It inherits uncertainty from ALS-to-AGB conversion, field and forest-inventory biomass equations, plot geolocation, regional inventory protocols, spatial aggregation to 1 ha/100 m support, and mangrove AGB training estimates. These uncertainties should be quantified in the provenance table and propagated into any formal product-uncertainty layer. Spaceborne-lidar covariates: GEDI and ICESat-2 canopy-height aggregates provide useful structural context where valid data exist, but their absence outside sampling footprints or valid acquisition periods should be treated as missing ancillary information rather than absence of target labels. Cloud and phenology: Despite quality filtering, persistent cloud cover in tropical regions and phenological variability introduce noise into annual optical composites. Temporal gaps: Pre-2010 estimates and regions with sparse reference labels remain more uncertain because model predictions depend more heavily on temporal extrapolation of remote-sensing relationships and regional transfer. Users should treat early-period estimates as indicative of long-term trends rather than precise annual stock assessments.

5.3 Comparison with Existing Products and Model Choice Revisited

Compared to existing products, this dataset offers three distinguishing features. Temporal depth: At 26 years (2000–2025), it exceeds CCI Biomass v6.0 (2007–2022 mapped epochs), JPL 2020 (single epoch), and NCEO Africa (mapped epochs in 2007–2010 and 2015–2020), enabling analysis of pre-GEDI dynamics and multi-decadal trend attribution. Methodological integration: The DenseNet architecture with 3 × 3 spatial

context windows represents a departure from the semi-empirical backscatter inversion (CCI), boosted-tree (JPL), and Random Forest (ICESat-2 Boreal, NCEO) approaches used in prior products. DenseNet's feature concatenation mechanism preserves multi-sensor feature diversity more effectively than additive residual connections, while the 3 × 3 window explicitly models spatial autocorrelation that tree-based methods treat only indirectly through spatial covariates. Disturbance preservation: The buffered mask-aware temporal harmonization explicitly separates stable pixels from disturbed pixels during cross-year calibration, preserving genuine change signals that uniform smoothing would erase.

The choice of DenseNet over alternative architectures merits reflection in light of the results. The validation $R^2 = 0.741$ and RMSE = 59.5 Mg ha^{-1} are comparable to the ICESat-2 Boreal product ($R^2 = 0.74$, RMSE = 59 Mg ha^{-1}), which used Random Forest, suggesting that input-data quality and label diversity may be as important as architecture choice. DenseNet remains appropriate here because it supports efficient end-to-end training and tiled GPU inference on large image stacks, while dense connectivity provides implicit regularization that can reduce overfitting in heterogeneous limited-sample settings. A controlled ablation on identical training/test splits comparing DenseNet, ResNet-18, and gradient boosted trees (XGBoost) is needed before making architecture-specific performance claims.

5.4 Implications for Carbon Monitoring

This product enables exploratory REDD+ MRV and national inventory analysis by providing hectare-scale AGB estimates that align with national forest management units and jurisdictional reporting boundaries. The 100-m resolution aligns with the GCOS breakthrough horizontal-resolution benchmark for AGB products, while the 26-year temporal depth supports baseline establishment and trend attribution relevant to the Paris Agreement Global Stocktake. Integration with national forest inventories is facilitated by the wall-to-wall coverage and annual temporal resolution, enabling comparison and potential fusion with plot-based estimates. For formal Tier 2–3 reporting, the product should be used with public processing provenance, uncertainty documentation, spatial-block validation, and country-specific calibration or comparison against national forest inventory plots. The RGB change composites offer a compact communication tool for policymakers, providing immediate visual evidence of forest dynamics across multi-decadal timeframes when paired with geographic context (coordinates, insets, and labeled landmarks).

6. Conclusion

This paper presents a global wall-to-wall AGB product at 100 m native spatial resolution spanning 2000–2025, achieved through DenseNet-based deep learning fusion of Landsat optical time series, ALOS PALSAR L-band SAR, ancillary GEDI and ICESat-2 canopy-height metrics, and topographic ancillary data (European Space Agency, 2021), trained against independent AGB labels compiled from ALS-derived 1-ha AGB products, field-plot and forest-inventory samples, selected regional/national inventory data, and mangrove AGB reference data. The product achieves $R^2 = 0.741$ and RMSE = 59.5 Mg

ha^{-1} on a sample-level held-out validation/test set, captures known regional patterns of deforestation, degradation, and regrowth, and provides a candidate dataset for sub-kilometer carbon accounting after additional spatial validation and release of processing provenance. The 3 × 3 spatial context window and DenseNet architecture were selected to exploit spatial autocorrelation in forest structure and mitigate overfitting in the heterogeneous, limited-sample regime of multi-source AGB reference data; validation results suggest the approach is competitive with existing methods while offering a scalable path to global, multi-decadal inference. Future work should incorporate ESA Biomass P-band SAR as appropriate to improve saturation behavior in high-biomass forests, add spatial block validation, extend to near-real-time operational processing, and develop ensemble uncertainty quantification to support robust carbon stock reporting under IPCC Tier 3 requirements.

Acknowledgements

This research was made possible by open data from NASA (Landsat, GEDI, ICESat-2, HLS), JAXA (ALOS PALSAR), ESA (Copernicus DEM, Sentinel-2), the University of Maryland (Hansen GFC), the Joint Research Centre (TMF), and the Chinese Academy of Sciences (GABAM), as well as ALS-derived AGB reference products, field-plot and forest-inventory datasets from the research community and selected regional/national inventories, and mangrove AGB training datasets contributed by coastal-region data providers.

Data Availability

Public access to the global 100 m AGB maps (2000–2025) is available at: https://doi.org/10.82924/7vmb-zv66. Public input datasets include Landsat (USGS EarthExplorer), GEDI (NASA Earthdata), ICESat-2 (NSIDC), ALOS PALSAR (JAXA ALOS Portal), Copernicus DEM (AWS Open Data), Hansen GFC (Google Earth Engine), GABAM (Zenodo), and JRC TMF (JRC Data Portal); reference-label sources will be listed separately with licensing and redistribution status.

References

Avitabile, V., Herold, M., Heuvelink, G. B. M., Lewis, S. L., Phillips, O. L., Asner, G. P., et al. (2016). An integrated pan-tropical biomass map using multiple reference datasets. Global Change Biology, 22(4), 1406–1420. https://doi.org/10.1111/gcb.13139

Baccini, A., Goetz, S. J., Walker, W. S., Laporte, N. T., Sun, M., Sulla-Menashe, D., et al. (2012). Estimated carbon dioxide emissions from tropical deforestation improved by carbon-density maps. Nature Climate Change, 2(3), 182–185. https://doi.org/10.1038/nclimate1354

Buchhorn, M., Smets, B., Bertels, L., De Roo, B., Lesiv, M., Tsendbazar, N.-E., et al. (2020). Copernicus global land service: Land cover 100m: Collection 3: Epoch 2019: globe. Zenodo. https://doi.org/10.5281/zenodo.3939050

Chander, G., Markham, B. L., & Helder, D. L. (2009). Summary of current radiometric calibration coefficients for Landsat MSS, TM, ETM+, and EO-1 ALI sensors. Remote Sensing of Environment, 113(5), 893–903. https://doi.org/10.1016/j.rse.2009.01.007

Chaplin-Kramer, R., Ramler, I., Sharp, R., Haddad, N. M., Gerber, J. S., West, P. C., et al. (2015). Degradation in carbon stocks near tropical forest edges. Nature Communications, 6, 10158. https://doi.org/10.1038/ncomms10158

Chen, C., Park, T., Wang, X., Piao, S., Xu, B., Chaturvedi, R. K., et al. (2019). China and India lead in greening of the world through land-use management. Nature Sustainability, 2, 122–129. https://doi.org/10.1038/s41893-019-0220-7

Claverie, M., Ju, J., Masek, J. G., Dungan, J. L., Vermote, E. F., Roger, J.-C., et al. (2018). The Harmonized Landsat and Sentinel-2 surface reflectance data set. Remote Sensing of Environment, 219, 145–161. https://doi.org/10.1016/j.rse.2018.09.002

Committee on Earth Observation Satellites. (2024). NCEO Africa Aboveground Woody Biomass 2020. CEOS Biomass Product Validation Good Practices Protocol. https://lpvs.gsfc.nasa.gov/Products/NCEO/NCEO_home.html

Dubayah, R., Blair, J. B., Goetz, S. J., Fatoyinbo, L., Hansen, M., Healey, S., et al. (2020). The Global Ecosystem Dynamics Investigation: High-resolution laser ranging of the Earth's forests and topography. Science of Remote Sensing, 1, 100002. https://doi.org/10.1016/j.srs.2020.100002

Duncanson, L., Neuenschwander, A., Hancock, S., Thomas, N., Fatoyinbo, L., Simard, M., et al. (2023). Boreal aboveground biomass density and uncertainty estimates from ICESat-2 and harmonized Landsat-Sentinel-2, 2020. ORNL DAAC. https://doi.org/10.3334/ORNLDAAC/2186

European Space Agency. (2021). Copernicus DEM: Global and European Digital Elevation Model. https://doi.org/10.5270/ESA-c5d3d65

Food and Agriculture Organization of the United Nations. (2025). Global Forest Resources Assessment 2025. Rome: FAO. https://doi.org/10.4060/cd6709en

Global Climate Observing System. (2022). The 2022 GCOS ECVs requirements (GCOS–245). World Meteorological Organization. https://library.wmo.int/idurl/4/58111

Hansen, M. C., Potapov, P. V., Moore, R., Hancher, M., Turubanova, S. A., Tyukavina, A., et al. (2013). High-resolution global maps of 21st-century forest cover change. Science, 342(6160), 850–853. https://doi.org/10.1126/science.1244693

Harris, N. L., Gibbs, D. A., Baccini, A., Birdsey, R. A., de Bruin, S., Farina, M., et al. (2021). Global maps of twenty-first century forest carbon fluxes. Nature Climate Change, 11, 234–240. https://doi.org/10.1038/s41558-020-00976-6

Healey, S. P., Yang, Z., Gorelick, N., Ilyushchenko, S., & Dubayah, R. (2023). GEDI L4B gridded aboveground biomass density, version 2.1. NASA EOSDIS Land Processes DAAC. https://doi.org/10.5067/GEDI/GEDI04_B.002

Huang, G., Liu, Z., van der Maaten, L., & Weinberger, K. Q. (2017). Densely connected convolutional networks. In Proceedings of the IEEE Conference on Computer Vision and Pattern Recognition (pp. 4700–4708). https://doi.org/10.1109/CVPR.2017.243

Intergovernmental Panel on Climate Change. (2019). 2019 refinement to the 2006 IPCC guidelines for national greenhouse gas inventories. IPCC. https://www.ipcc-nggip.iges.or.jp/public/2019rf/

Kattenborn, T., Leitloff, J., Schiefer, F., & Hinz, S. (2021). Review on convolutional neural networks (CNN) in vegetation remote sensing. ISPRS Journal of Photogrammetry and Remote Sensing, 173, 24–49. https://doi.org/10.1016/j.isprsjprs.2020.12.010

Lang, N., Jetz, W., Schindler, K., & Wegner, J. D. (2023). A high-resolution canopy height model of the Earth. Nature Ecology & Evolution, 7, 1778–1789. https://doi.org/10.1038/s41559-023-02206-6

Long, T., Zhang, Z., He, G., Jiao, W., Tang, C., Wu, B., et al. (2019). 30 m resolution global annual burned area mapping based on Landsat images and Google Earth Engine. Remote Sensing, 11(5), 489. https://doi.org/10.3390/rs11050489

Zhang, Z., Qi, B., Long, T., He, G., & Wei, M. (2025). Updated 30 m resolution global annual burned area map, 2014–2024 (Version v3) [Data set]. Zenodo. https://doi.org/10.5281/zenodo.17707433

Neuenschwander, A. L., & Pitts, K. L. (2019). The ATL08 land and vegetation product for the ICESat-2 Mission. Remote Sensing of Environment, 221, 247–259. https://doi.org/10.1016/j.rse.2018.11.005

Pan, Y., Birdsey, R. A., Phillips, O. L., Houghton, R. A., Fang, J., Kauppi, P. E., et al. (2024). The enduring world forest carbon sink. Nature, 631, 563–569. https://doi.org/10.1038/s41586-024-07602-x

Potapov, P., Li, X., Hernandez-Serna, A., Tyukavina, A., Hansen, M. C., Kommareddy, A., et al. (2021). Mapping global forest canopy height through integration of GEDI and Landsat data. Remote Sensing of Environment, 253, 112165. https://doi.org/10.1016/j.rse.2020.112165

Roy, D. P., Wulder, M. A., Loveland, T. R., Woodcock, C. E., Allen, R. G., Anderson, M. C., et al. (2014). Landsat-8: Science and product vision for terrestrial global change research. Remote Sensing of Environment, 145, 154–172. https://doi.org/10.1016/j.rse.2014.02.001

Saatchi, S. S., Harris, N. L., Brown, S., Lefsky, M., Mitchard, E. T. A., Salas, W., et al. (2011). Benchmark map of forest carbon stocks in tropical regions across three

continents. Proceedings of the National Academy of Sciences, 108(24), 9899–9904. https://doi.org/10.1073/pnas.1019576108

Saatchi, S. S., Marlier, M., Chazdon, R. L., Clark, D. B., & Russell, A. E. (2011). Impact of spatial variability of tropical forest structure on radar estimation of aboveground biomass. Remote Sensing of Environment, 115(11), 2836–2849. https://doi.org/10.1016/j.rse.2010.07.015

Saatchi, S. S., Mascaro, J., Xu, L., Keller, M., Yang, Y., Duffy, P., et al. (2015). Seeing the forest beyond the trees. Global Ecology and Biogeography, 24(5), 606–610. https://doi.org/10.1111/geb.12256

Santoro, M., & Cartus, O. (2025). ESA Biomass Climate Change Initiative (Biomass_cci): Global datasets of forest above-ground biomass for 2007, 2010 and 2015–2022, v6.0. NERC EDS Centre for Environmental Data Analysis. https://doi.org/10.5285/62f15a556db8428186f78d0a17e75615

Santoro, M., Cartus, O., Carvalhais, N., Rozendaal, D. M. A., Avitabile, V., Araza, A., et al. (2021). The global forest above-ground biomass pool for 2010 estimated from high-resolution satellite observations. Earth System Science Data, 13, 3927–3950. https://doi.org/10.5194/essd-13-3927-2021

Shimada, M., Itoh, T., Motooka, T., Watanabe, M., Shiraishi, T., Thapa, R., & Lucas, R. (2014). New global forest/non-forest maps from ALOS PALSAR data (2007–2010). Remote Sensing of Environment, 155, 13–31. https://doi.org/10.1016/j.rse.2014.04.014

Silva, C. A., Duncanson, L., Hancock, S., Neuenschwander, A., Thomas, N., Hofton, M., et al. (2021). Fusing simulated GEDI, ICESat-2 and NISAR data for regional aboveground biomass mapping. Remote Sensing of Environment, 253, 112234. https://doi.org/10.1016/j.rse.2020.112234

Tian, L., Wu, X., Tao, Y., Li, M., Qian, C., Liao, L., & Fu, W. (2023). Review of remote sensing-based methods for forest aboveground biomass estimation: Progress, challenges, and prospects. Forests, 14(6), 1086. https://doi.org/10.3390/f14061086

UK Government. (2021). Glasgow Leaders' Declaration on Forests and Land Use. https://ukcop26.org/glasgow-leaders-declaration-on-forests-and-land-use/

Vancutsem, C., Achard, F., Pekel, J.-F., Vieilledent, G., Carboni, S., Simonetti, D., et al. (2021). Long-term (1990–2019) monitoring of forest cover changes in the humid tropics. Science Advances, 7(10), eabe1603. https://doi.org/10.1126/sciadv.abe1603

Wang, J. A., Baccini, A., Farina, M., Randerson, J. T., & Friedl, M. A. (2021). Disturbance suppresses the aboveground carbon sink in North American boreal forests. Nature Climate Change, 11, 435–441. https://doi.org/10.1038/s41558-021-01027-4

Xu, L., Saatchi, S. S., Yang, Y., Yu, Y., Pongratz, J., Bloom, A. A., et al. (2021). Changes in global terrestrial live biomass over the 21st century. Science Advances, 7(27), eabe9829. https://doi.org/10.1126/sciadv.abe9829

Yang, Y., Saatchi, S. S., Xu, L., Yu, Y., Choi, S., Phillips, N., et al. (2018). Post-drought decline of the Amazon carbon sink. Nature Communications, 9, 3172. https://doi.org/10.1038/s41467-018-05668-6

Yang, Y., Saatchi, S., Xu, L., Keller, M., Corsini, C. R., Aragão, L. E. O. C., et al. (2020). Interannual variability of carbon uptake of secondary forests in the Brazilian Amazon (2004–2014). Global Biogeochemical Cycles, 34, e2019GB006396. https://doi.org/10.1029/2019GB006396

Yang, G., Crowther, T. W., Lauber, T., Zohner, C. M., Smith, G. R., et al. (2025). A globally consistent negative effect of edge on aboveground forest biomass. Nature Ecology & Evolution, 9, 2036–2045. https://doi.org/10.1038/s41559-025-02840-2

Yu, Y., Saatchi, S., Yang, Y., Xu, L., Meyer, V., et al. (2025). Mapping Global Live Woody Vegetation Biomass at Optimum Spatial Resolutions (Version v2) [Data set]. Zenodo. https://doi.org/10.5281/zenodo.15858551

Zhu, Z., & Woodcock, C. E. (2012). Object-based cloud and cloud shadow detection in Landsat imagery. Remote Sensing of Environment, 118, 83–94. https://doi.org/10.1016/j.rse.2011.10.028